How to cite: *Angew. Chem. Int. Ed.* **2022,** *61,* e202116194
International Edition: doi.org/10.1002/anie.202116194
German Edition: doi.org/10.1002/ange.202116194

Aluminium–Amine Battery

An Efficient Rechargeable Aluminium–Amine Battery Working Under Quaternization Chemistry

*Gang Wang, Evgenia Dmitrieva, Benjamin Kohn, Ulrich Scheler, Yannan Liu, Valeriya Tkachova, Lin Yang, Yubin Fu, Ji Ma, Panpan Zhang, Faxing Wang, Jin Ge, and Xinliang Feng**

Abstract: *Rechargeable aluminium (Al) batteries (RABs) have long-been pursued due to the high sustainability and three-electron-transfer properties of Al metal. However, limited redox chemistry is available for rechargeable Al batteries, which restricts the exploration of cathode materials. Herein, we demonstrate an efficient Al–amine battery based on a quaternization reaction, in which nitrogen (radical) cations ($R_3N^{\bullet+}$ or R_4N^+) are formed to store the anionic Al complex. The reactive aromatic amine molecules further oligomerize during cycling, inhibiting amine dissolution into the electrolyte. Consequently, the constructed Al–amine battery exhibits a high reversible capacity of 135 mAh g^{-1} along with a superior cycling life (4000 cycles), fast charge capability and a high energy efficiency of 94.2 %. Moreover, the Al–amine battery shows excellent stability against self-discharge, far beyond conventional Al–graphite batteries. Our findings pave an avenue to advance the chemistry of RABs and thus battery performance.*

[*] Dr. G. Wang, Dr. Y. Liu, Dr. V. Tkachova, L. Yang, Dr. Y. Fu, Dr. J. Ma, Dr. P. Zhang, Dr. F. Wang, Prof. X. Feng
Center for Advancing Electronics Dresden (cfaed), Faculty of Chemistry and Food Chemistry, Technische Universität Dresden
01062 Dresden (Germany)
E-mail: xinliang.feng@tu-dresden.de

Dr. E. Dmitrieva, Dr. J. Ge
Leibniz-Institut für Festkörper- und Werkstoffforschung Dresden (IFW) e.V.
Helmholtzstraße 20
01069 Dresden (Germany)

B. Kohn, Dr. U. Scheler
Leibniz-Institut für Polymerforschung Dresden e.V.
01069 Dresden (Germany)

Dr. P. Zhang
Current address: State Key Laboratory of Materials Processing and Die & Mould Technology, School of Materials Science and Engineering, Huazhong University of Science and Technology, 430074 Wuhan, China.

Introduction

Sustainable and efficient energy storage technologies are highly desirable to meet ever-increasing energy demands in today's world.[1] Rechargeable aluminium (Al) batteries (RABs) that promise to deliver high energy and sustainability at low cost stand out among various batteries.[2] Al is the most abundant metal element (8.1 wt%) in the Earth's crust, and possesses both high theoretical volumetric (8056 mAh cm^{-3}) and gravimetric (2981 mAh g^{-1}) capacity with ease in processing and recycling. Currently, RABs are still in their infancy, and the development of suitable redox chemistry in which Al charge carriers (Al^{3+}, $Al_xCl_y^-$ and $AlCl_z^{n+}$) reversibly participate remains a great challenge.

The high-energy chalcogen cathodes (O^0/O^{2-} and S^0/S^{2-}) interact strongly with Al^{3+},[3] making Al–O_2 batteries unrechargeable[4] and leading to poor kinetics and low stability of Al–S batteries.[5] Improved Al^{3+} diffusion kinetics was achieved lately in amorphous TiS_4 under S^-/S^{2-} conversion.[6] In contrast to Al^{3+}, anionic Al complexes ($Al_2Cl_7^-$ and $AlCl_4^-$) in ionic liquid show impressively high diffusion coefficients and smooth Al plating–stripping behavior, enabling Al-graphite/graphene batteries based on anion intercalation chemistry of graphitic carbon (C_n^0/C_n^+).[7] Nevertheless, there exists a self-discharge[8] problem of Al–carbon batteries, which is probably due to the electrolyte decomposition and/or weak ionic bonding between anion and carbon hosts. More recently, cationic Al complexes ($AlCl_2^+$ and $AlCl^{2+}$)[2b,9] have been demonstrated as a new type of charge species in Al–ketone and Al–quinone batteries, in which carbonyl oxygen chelates $AlCl_2^+$ and $AlCl^{2+}$ via C=O/C–O^- transformation. Despite the use of polyquinone, a continuous capacity fading is still presented,[10] which is likely caused by a deterioration of the structure[11] during repeated carbonyl bonding cleavage and re-formation. Therefore, it is highly appealing to explore further redox chemistry, while addressing the aforementioned kinetic and stability issues (self-discharge and capacity fading) that are prevalently suffered in todays' RABs.

Herein, we demonstrate a quaternization chemistry for RABs using a family of aromatic amines as the cathode materials. The quaternization of amine during oxidation entails the formation of N (radical) cations ($R_3N^{\bullet+}$ or R_4N^+) and reversible storage of anionic aluminium complex ($AlCl_4^-$). The phenyl substituents play a key role in

stabilizing the resulting N radical cations by electron delocalization, endowing the amine molecules with high redox activity (fast kinetics and high capacity). Further oligomerization of the reactive amine molecules during cycling inhibits dissolution into the electrolyte, making the amine electrodes highly reversible, efficient and stable for anion storage. As the result, the assembled Al–amine battery delivers a high reversible capacity of 135 mAh g^{-1}, a high energy efficiency (EE) of 94.2 %, a long cycling life over 4000 cycles, fast charge capability (3 min), together with notable features, such as high loading capability and excellent stability against self-discharge.

Results and Discussion

Working Principle of Al–Amine Battery

The operation of Al–amine batteries relies on the quaternization of the amine compound at the cathode and Al plating/stripping at the anode (Figure 1). During the charging process, the amine compound is oxidized by losing electrons from the lone electron pairs in the N center, producing an amine radical cation ($R_3N^{\bullet+}$). In the case of a multi-N-containing amine compound, the free radical electrons will delocalize to form new conjugated configurations (e.g. quinone diiminium). In this regard, radicals will not be detected in the charged amine compound (R_4N^+). To maintain the charge neutrality of the electrode, Al complex anions ($AlCl_4^-$) will be inserted into the cathode. Simultaneously, Al metal is deposited on the anode via $Al_2Cl_7^-/AlCl_4^-$ conversion.[7a] Reverse reactions take place during the discharging process. The proposed amine molecules include triphenylamine (**N1**), 1,4-bis(diphenylamino)benzene (**N2**), 1,3,5-tris(diphenylamino)benzene (**N3**), and 4,4′,4′′-tris(diphenylamino)triphenylamine (**N4**) with different numbers of N centers (Figure 1). All these aromatic amine compounds have a 3D conformation in which each N center is spatially separated to ensure the accessibility of redox centers.[12] Based on one-electron transfer per N center, the calculated theoretical capacities of **N1**–**N4** range from 109 to144 mAh g^{-1} (Table S1).

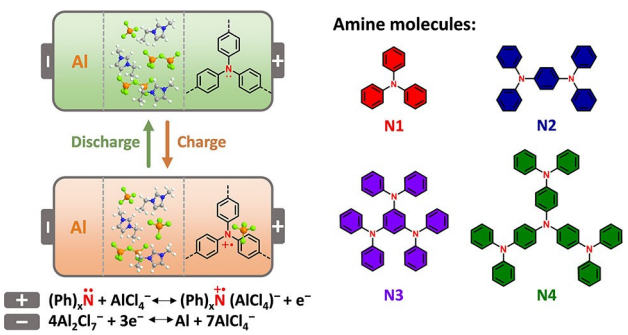

Figure 1. Working principle of the Al–amine battery and the proposed aromatic amine molecules. Ph represents phenyl groups.

Electrochemical Behavior and Characterization of Amine Molecules

Swagelok cells with a tungsten (W) rod (Figure S1) were used to evaluate the electrochemical performance of aromatic amine compounds in RABs. Al ionic liquid ($AlCl_3$/EMImCl = 1.3, denoted as IL-1.3) was employed as the electrolyte (Figure S2). The working electrodes were prepared by mixing amine molecules, carbon additive and alginate sodium binder in a mass ratio of 80:10:10 with W foil or carbon cloth as the current collector. It was confirmed that all these electrode components (carbon additive, binder, W foil and carbon cloth) were redox-inactive (without contributing to any redox peaks) in a wide voltage window of 0–2.4 V (Figure S3).

Within a voltage window of 0.2–1.85 V, galvanostatic measurements of amine molecules were carried out against Al metal at 0.1 A g^{-1}. We noticed different cycling behavior: **N1** and **N2** presented single and double plateaus around 1 V in the charge–discharge curves (Figure S4A, B), but showed fast fading capacities (Figure 2A), which are ascribed to the severe dissolution of the active material into the electrolyte, as evidenced by the deep color of the separator after cycling test (Figure S5). Compared to **N1** and **N2**, improved capacity (40 mAh g^{-1}) was achieved on **N3** due to the relatively larger molecule associated with less solubility. In contrast, an activation process was recognized for **N4** with significant capacity enhancement during the initial 25 cycles (Figure 2A, B), and the capacity stabilized around 135 mAh g^{-1} with a Coulombic efficiency (CE) of 99.9 % (Figure S4D), corresponding to 93 % active site utilization based on its theoretical capacity. Several small plateaus appeared in the initial charge–discharge curves (Figure 2B), suggesting a multi-electron transfer mechanism. Then, the charge–discharge profiles evolved into sloping curves with an average working voltage of 1.1 V, which deviated far from the flat potential plateaus as observed in classic phase-transition cathode.[13] In addition, the activation process was accompanied with morphology variation in **N4** electrode, where **N4** micro-rods in the original electrode disappeared and turned into a compact electrode (Figure S6). This result suggests that the electrochemical reaction of **N4** proceeds in bulk phase rather than merely on surface, contributing to the high active site utilization.

To track the activation process of **N4**, we carried out CV measurements in the same voltage range. Three main oxidation peaks located at 0.92, 1.38 and 1.64 V showed up in the first anodic scan along with a shoulder peak at 0.8 V, while four reduction peaks at 1.42, 1.24, 0.88 and 0.62 V followed in the subsequent cathodic scan (Figure 2C), signifying that four-electron transfer was involved in the redox reaction. In the extended CV scans, the current density of redox peaks gradually strengthened, validating improved activity of **N4**. At the same time, all redox peaks progressively downshifted in position by ≈0.2 V, which implies a structure change of **N4**. The chemical identity of **N4** before and after the cycling test was further monitored by matrix-assisted laser desorption/ionization-time of flight (MALDI-TOF) mass spectroscopy. It was noted that high-

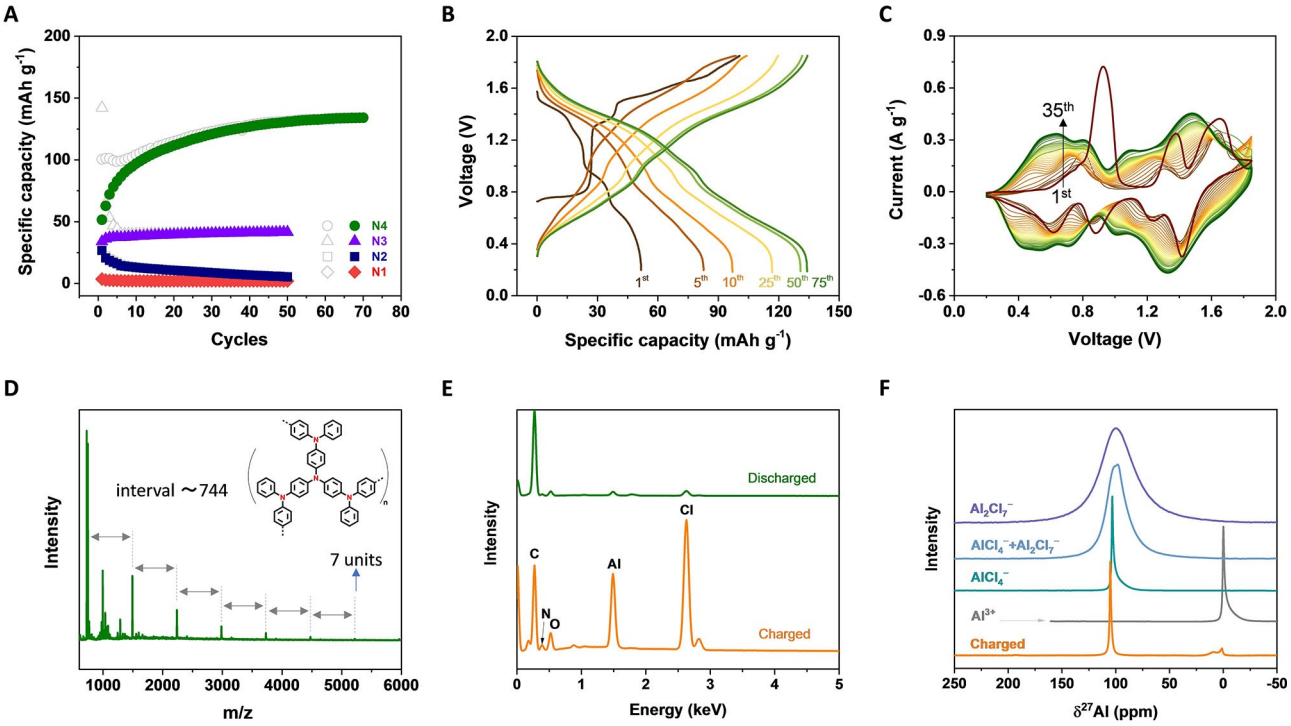

Figure 2. Electrochemical behavior and characterization of amine molecules. A) Cycling performance of different Al–amine cells at 0.1 A g^{-1}. The voltage window is 0.2–1.85 V vs. Al. Blank and filled symbols represent charge capacity and discharge capacity, respectively. B) Charge–discharge curves of the Al–**N4** cell at different cycles. C) First 35-cycle CV scans of the Al–**N4** cell. The scan rate is 1 mV s^{-1}. D) MALDI-TOF mass spectrum of cycled **N4** electrode. Inset is a proposed structure of **N4** oligomers. E) EDX spectra of fully charged and discharged $(\mathbf{N4})_n$ electrodes. F) NMR spectra of Al ionic liquid electrolytes (liquid-state NMR) and charged $(\mathbf{N4})_n$ electrode (solid-state NMR 25 kHz MAS).

molecular-weight **N4** oligomers (up to 5220 with 7 repeating units) were detected for the cycled electrode (Figure 2D), which contrasted with the pure **N4** monomer in the pristine electrode (Figure S7). The *m*/*z* intervals are determined as ≈744, which is well consistent with the mass of **N4** building block eliminating three hydrogen atoms. The signals in the range of *m*/*z* 1000–1300 originates from alginate sodium binder (Figure S8). It is evident that **N4** monomer in situ oligomerized during the cycling process, resulting in a downshift of the redox potential, as confirmed by density functional theory calculation (Figure S9). Hereafter, the **N4** oligomers are denoted as $(\mathbf{N4})_n$ for easy identification.

Fourier transform infrared (FTIR) spectroscopy further reveals that oligomerization of **N4** preserves redox active N centers because of the maintenance of characteristic peaks of C–N stretching at 1257 cm^{-1} and C–C ring stretching at 1586 cm^{-1} in the formed $(\mathbf{N4})_n$ (Figure S10A). X-ray diffraction (XRD) measurement indicates that the formed $(\mathbf{N4})_n$ has an amorphous structure (Figure S10B), which is likely the reason for the lack of flat potential plateaus in the charge–discharge profiles. Besides, it was also found that the oligomerization of aromatic amine compound was related to the terminal group of the amine. When another four-N-center amine molecule, 4,4′,4″-tri-9-carbazolyltriphenylamine (**N4′**), was used under the same condition, no oligomerization was observed after cycling (Figure S11). It is worth noting that the **N4′** delivered both an inferior capacity (115 mAh g^{-1}) and CE (< 90 %).

To confirm that anion participates into the operation of Al–amine batteries, energy dispersive X-ray analysis (EDX) was performed on the fully charged (1.85 V vs. Al) and discharged $(\mathbf{N4})_n$ electrodes (0.2 V vs. Al). Substantial Al and Cl signals arose on the fully charged sample (Figure 2E) and were uniformly distributed throughout the electrode (Figure S12), whereas negligible Al and Cl signals remained in the discharged sample, verifying the anion insertion/extraction. ^{27}Al nuclear magnetic resonance spectroscopy (NMR)[14] was further utilized to probe the inserted anion species in the charged $(\mathbf{N4})_n$ electrode. Three Al electrolytes (IL-1, IL-1.3 and IL-2), which contain $AlCl_4^-$, $AlCl_4^- + Al_2Cl_7^-$ and presumably $Al_2Cl_7^-$, respectively, generate three peaks with slight shift and different line width (100 Hz to 3255 Hz) on the liquid ^{27}Al NMR spectra (Figure 2F). Among three anion compositions ($AlCl_4^-$, $AlCl_4^- + Al_2Cl_7^-$ and presumably $Al_2Cl_7^-$), $AlCl_4^-$ showed the finest signal at 103.2 ppm. For the charged $(\mathbf{N4})_n$ electrode, the solid-state ^{27}Al NMR spectrum showed strong resonance at 105.0 ppm, which is as sharp as $AlCl_4^-$ in liquid electrolyte (IL-1). No evidence of $Al_2Cl_7^-$ is present in the charged cathode. This result suggests that $AlCl_4^-$ is the inserted species in the charged electrode. The changed chemical shift from 103.2 to 105.0 ppm is indicative of the interaction between $AlCl_4^-$ and N cation site ($N^{\bullet+}$ and N^+ explained in later section) in the charged electrode. A tiny peak was noticed around 5 ppm, which is assigned to $Al(OH)_{3-x}O_{3-x/3}$[14a] due to short moisture/air contact during sample transfer.

Confirmation of Electrochemical Quaternization of N4

To gain insights into the reaction processes and redox intermediates of **N4**, electrochemistry (EC) and spectroelectrochemistry (SEC) were executed by collecting time-resolved and in situ electrochemical and spectroscopic information. Because of limited solubility of **N4** in Al ionic liquid electrolyte, direct SEC measurement in Al ionic liquid failed. As an alternative, we conducted EC and SEC measurements in a three-electrode system in dichloromethane containing 0.1 M tetrabutylammonium hexafluorophosphate ($TBAPF_6$) (appropriate electrolyte for **N4** study) with **N4** completely dissolved. The reaction extent was first controlled to be a two-electron oxidation (**N4**↔$\mathbf{N4}^{2+}+2e^-$), where cyclic voltammogram of **N4** shows two reversible one-electron processes at −0.1 and 0.26 V vs Fc/Fc^+ (Figure 3A). The potential difference of anodic and cathodic peaks ranges from 75 to 100 mV under wide scan rates of 10–

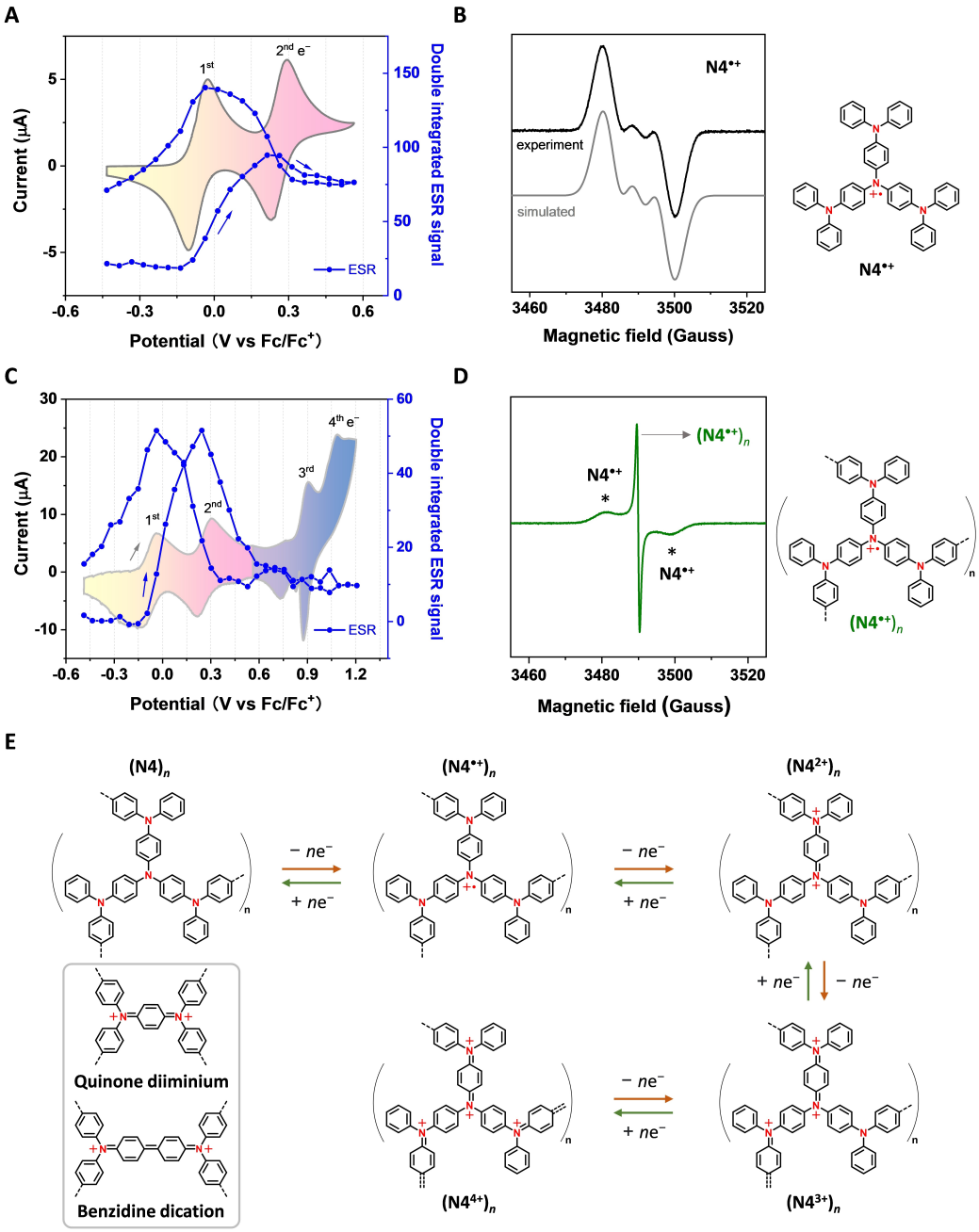

Figure 3. ESR SEC measurements on **N4** dissolved in dichloromethane (0.1 M $TBAPF_6$). A) CV and evolution of the ESR signal intensity as a function of potential under a two-electron oxidation. The potentials are given versus the Fc/Fc^+ couple. The scan rate is 2.5 $mV\,s^{-1}$. B) ESR spectrum and structure of **N4** radical cation ($\mathbf{N4}^{\bullet+}$). C) CV and evolution of the ESR signal intensity as a function of potential under a four-electron oxidation. D) ESR spectrum and structure of $(\mathbf{N4})_n$ radical cation ($(\mathbf{N4}^{\bullet+})_n$). E) The proposed energy storage process of $(\mathbf{N4})_n$. Anion is omitted in the reaction.

1000 mV s^{-1} (Figure S13A), indicating high reversibility and intrinsically fast kinetics. The electron spin resonance (ESR) SEC of **N4** showed a signal with a *g* value of 2.003 (Figure 3B) and a hyperfine splitting ($a(^{14}N) = 6.8$ Gauss) caused by the interaction of the unpaired electron spin with the spin of nitrogen nucleus. The unpaired electron in the radical is located on the central nitrogen atom. The ESR intensity increased during the first redox peak in CV and decreased during the second one (Figure 3A), implying the first formation of paramagnetic **N4** radical cation ($\mathbf{N4}^{\bullet+}$) and subsequent conversion into ESR-silent dication ($\mathbf{N4}^{2+}$). Closed-shell quinone diiminium ($\mathbf{N4}^{2+}$) is proposed as the most plausible oxidized form (Figure S13E) due to its lower energy than open-shell dication diradicals based on DFT calculations (Figure S14, S15). The ultraviolet-visible-near infrared (UV/Vis-NIR) absorption bands of $\mathbf{N4}^{\bullet+}$ and $\mathbf{N4}^{2+}$ are presented in Figure S13C.

Upon elevating the potential window to exert full redox capability ($\mathbf{N4} \leftrightarrow \mathbf{N4}^{4+} + 4e^-$) of **N4**, the third and fourth redox processes become irreversible (Figure 3C and S16). The reduction waves in the potential range from 0.6 to 1.2 V correspond to the reduction processes of the new formed species (redox pair at 0.75 V) as well as to the adsorption of charged species on the electrode surface (a sharp peak at 0.9 V). The in situ ESR spectra measured during the 6th voltammetric cycle demonstrated two superimposed signals (Figure 3D): a broad signal of the **N4** radical cation ($\mathbf{N4}^{\bullet+}$, marked by asterisk) and a new signal with a *g* value of 2.003 and a line width of 0.8 Gauss. The appearance of a narrow ESR signal suggests the formation of the radical in an extended π-system as oligomers ($(\mathbf{N4}^{\bullet+})_n$).[15] At the potential of the third redox event (Figure 3C), a very weak ESR signal was obtained which can be assigned to the radical trication species. The radical trication likely undergoes oligomerization reaction through the C–C coupling between two **N4** molecules by eliminating protons on *para*-phenyl position since peripheral phenyl rings in **N4** are reactive (Figure S18). Based on the above analysis, the nitrogen atom performs as the redox active site of aromatic amine by forming N (radical) cation ($N^{\bullet+}$ and N^+), while **N4** oligomerization is initiated after the third electron transfer and further cycling deepens oligomerization extent. In spite of four pairs of redox peaks appeared, the CV curves collected in SEC measurement (Figure 3C) differ in shape from those of Al-$(\mathbf{N4})_n$ cells (Figure 2C), which may correlate with the diffusion property and concentration difference of redox-active compounds (both **N4** and $(\mathbf{N4})_n$) in liquid and solid states.

Under the "real conditions" of an Al–amine battery, the Al ionic liquid electrolyte was used instead of $TBAPF_6$ electrolyte. The movements of **N4** molecule in solid electrode is restricted, thus the oligomerization takes time and shows a phenomenological behavior of activation (Figure 2A,B). The activated **N4** electrode also exhibited an ESR signal with a *g* value (2.003) and a line width (0.8 Gauss, Figure S19), implying that similar oligomer radical ($(\mathbf{N4}^{\bullet+})_n$) was formed. Because the oligomerization of **N4** is irreversible, thereafter, the electrochemical reaction of $(\mathbf{N4})_n$ electrode is proposed to proceed between the neutral $(\mathbf{N4})_n$ and fully charged $(\mathbf{N4}^{4+})_n$, where quinone diiminium and benzidine dication are involved during the multi-electron transfer process (Figure 3E).

Electrochemical Properties of the Al–$(N4)_n$ Battery

Voltage hysteresis (polarization) of cathode materials remains a major drawback of RABs,[16] which prevents EE from approaching integer (100 %). State-of-the-art Al–graphite/graphene batteries can only deliver a maximum EE of ≈85 %.[7a,17] In contrast, the constructed Al–$(\mathbf{N4})_n$ battery after conditioning cycles presented nearly overlapped charge–discharge profiles (Figure 4A) at a high active material ratio (80 %) and loading (3.5–4 mg cm^{-2}), both of which are much higher than those (30–50 %, 0.5–1.5 mg cm^{-2}) for high-performance Al–quinone,[2b,18] Al–pyrene[19] and Al–tetradiketone[9a] batteries. The voltage hysteresis of the Al–$(\mathbf{N4})_n$ battery was determined as low as 73 mV at 0.1 A g^{-1}, contributing to a record EE of 94.2 % in RABs (Figure 4B).

Further, the Ohmic resistance (R_s) of the Al–$(\mathbf{N4})_n$ battery was found sensitive to the state of charge (SOC) regardless of electrolyte amount or concentration (Figure S20, S21). The R_s decreased during charging (0 % to 75 % SOC) and recovered at the fully charged state (100 % SOC), displaying a valley-shape variation curve (Figure 4C). The reverse R_s variation occurred during discharging. The R_s change mainly originated from the $(\mathbf{N4})_n$ active materials (rather than from the electrolyte) and closely resembled that of redox salts or polymers under a mixed-valence conductivity mode,[20] where active materials showed conductivity except in the neutral and fully charged states. Under this model, charge transport within $(\mathbf{N4})_n$ is expected via electron hopping between intra- and inter-oligomer redox N sites (Figure S22). The reduced R_s of $(\mathbf{N4})_n$ during oxidation contributes to the low voltage hysteresis of the Al–$(\mathbf{N4})_n$ battery.

The galvanostatic intermittent titration technique (GITT) was used to examine the kinetics of reactions at different stages (Figure S23). The diffusion coefficients of $AlCl_4^-$ were estimated to be $4–9 \times 10^{-8}$ $cm^2 s^{-1}$ in the whole voltage window (Figure 4D), which is higher than 10^{-11}–10^{-9} $cm^2 s^{-1}$ of $AlCl_4^-$ diffusion in graphite[21] and highlights the fast kinetics of quaternization. Therefore, the Al–$(\mathbf{N4})_n$ battery exhibited excellent rate capability. High reversible capacities of 136, 124 and 116 mAh g^{-1} were achieved at 0.05, 1 and 2 A g^{-1} (Figure 4E), respectively, without generating much polarization on the charge–discharge profiles (Figure S24).

The long-term cycling stability of the Al–$(\mathbf{N4})_n$ battery was assessed at 1 A g^{-1}. As shown in Figure 4F, after 4000 cycles (≈40 days), the Al–$(\mathbf{N4})_n$ battery still maintained a capacity of 116 mAh g^{-1} corresponding to a capacity retention of 93.5 %. The CE averaged to 99.88 % during the cycling. Moreover, even at a high active material loading of 6 and 12.9 mg cm^{-2}, the Al–$(\mathbf{N4})_n$ battery demonstrated stable cycling performance and delivered high reversible capacities of 125–128 mAh g^{-1} at 0.1 A g^{-1} (Figure 4G). The

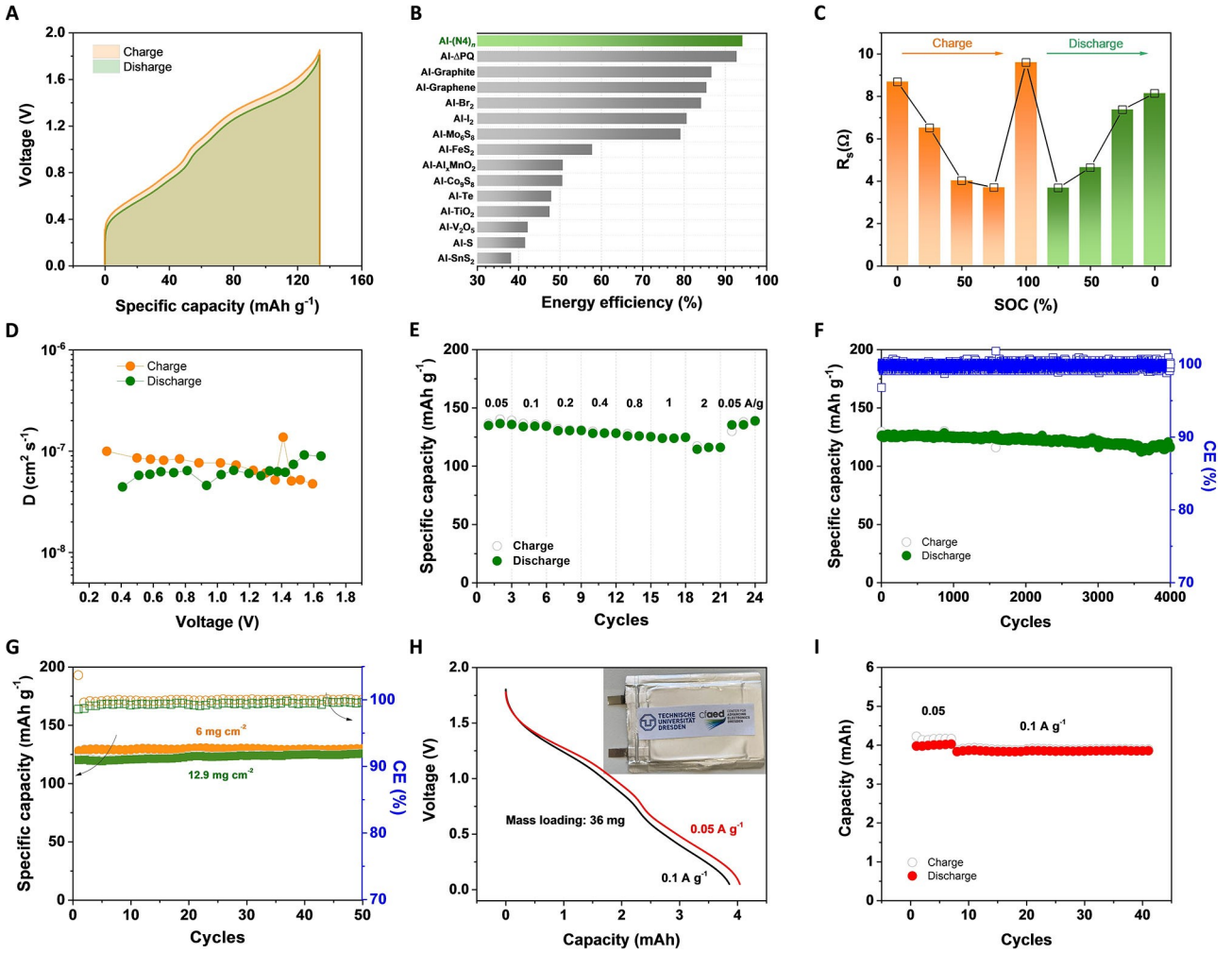

Figure 4. Electrochemical features of Al–(**N4**)$_n$ batteries. A) Typical charge–discharge profiles of the Al–(**N4**)$_n$ battery at 0.1 A g^{-1}. B) EE comparison of the Al–(**N4**)$_n$ battery with other RABs. C) R_s change of Al–(**N4**)$_n$ battery determined by EIS at different charging states. D) Diffusion coefficient of $AlCl_4^-$ in the (**N4**)$_n$ electrode determined by GITT. E) Rate performance of Al–(**N4**)$_n$ battery at 0.05–2 A g^{-1}. F) Long-term cycling of the Al–(**N4**)$_n$ battery at 1 A g^{-1}. G) Cycling performance of the Al–(**N4**)$_n$ battery at high loadings of 6 and 12.9 mg cm^{-2}. An extended voltage window of 0.1–2 V was used for 12.9 mg cm^{-2} loading to compensate polarization. H) Typical discharge curve of the Al–(**N4**)$_n$ battery with a capacity of 4 mAh. Inset is an optical photo of an Al–amine pouch cell. I) Cycling performance of the Al–(**N4**)$_n$ pouch cell.

Al–(**N4**)$_n$ battery also performed well in the IL-2 with a similar capacity (134 mAh g^{-1}) and an average discharge voltage of 1.05 V (Figure S25). Further, an Al–(**N4**)$_n$ pouch cell with a high mass loading of 36 mg was assembled, which could stably output a high capacity of 4 mAh (Figure 4H, I).

Self-Discharge Evaluation of the Al–(N4)$_n$ Battery

Self-discharge is a common yet underrated phenomenon associated with organic batteries[22] and anion-related energy,[23] especially when small organic molecules or high-voltage cathodes are used as active materials. Electron hopping between dissolved molecule[22] constitutes inner short circuit, while side reaction may cause additional electron transfer at high voltage used for anion storage, sacrificing both the EE and CE of energy devices. The self-discharge behavior of the Al–(**N4**)$_n$ battery was evaluated by resting the fully charged battery at open circuit for specific time (10–168 h), then the battery was fully discharged at a fixed current of 0.1 A g^{-1}. The Al–**N4′** battery and Al–graphite battery were tested for comparison. At room temperature (25 °C), the fully charged Al–(**N4**)$_n$ battery maintained 94.7 % capacity (126 vs. 133 mAh g^{-1}) after standing 2 days at open circuit (Figure 5A), which is much higher than 71.3 % (77 vs. 108 mAh g^{-1}) for Al-**N4′** battery under the same condition (Figure S27). Because **N4** was oligomerized while **N4′** did not, the capacity retention difference indicates the significance of oligomerization on suppressing self-discharge. Further extending the rest period of the Al–(**N4**)$_n$ battery from 2 to 7 days did not induce noticeable capacity loss. Decent capacities of 111, 94 and 79 mAh g^{-1} were still achieved at 50 °C, 75 °C and 100 °C (Figure 5B and S26), respectively. Note that those performance were collected with the cells rested and cycled under specific temperatures. The Al–graphite battery, however,

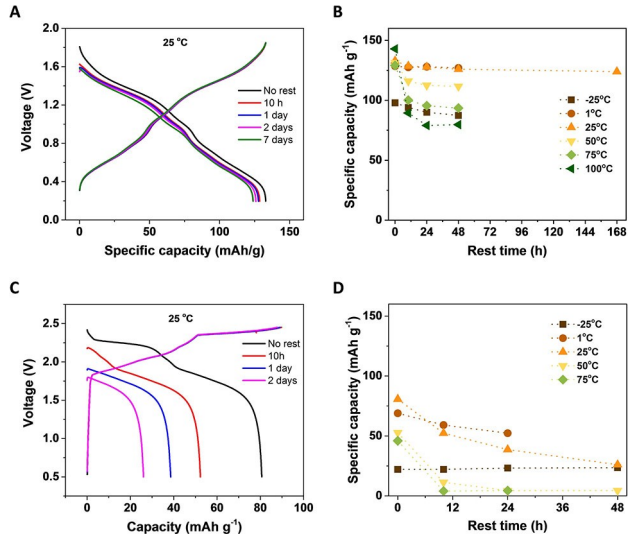

Figure 5. Self-discharge test of the Al–(**N4**)$_n$ battery and Al–graphite battery. A) Self-discharge test of the Al–(**N4**)$_n$ battery at 25 °C. B) Capacity retention of the Al–(**N4**)$_n$ battery under different temperatures. C) Self-discharge test of the Al–graphite battery at 25 °C. D) Capacity retention of the Al–graphite battery under different temperatures.

suffered from a serious self-discharge with low capacities of 5–26 mAh g^{-1} retained (Figure 5C,D and S28) under the same conditions (25–75 °C). The excellent anti-self-discharge behavior of the Al–(**N4**)$_n$ battery can be ascribed to the low solubility of (**N4**)$_n$, strong ionic bonding between $AlCl_4^-$ and N cation sites, and medium working voltage.

Conclusion

We have introduced the new quaternization chemistry for Al batteries, employing aromatic amine compounds as cathode materials. The quaternization of amine was confirmed by in situ EC and SEC measurements, and $AlCl_4^-$ was determined as the inserted charge carriers into amine cathodes in RABs. The constructed Al–(**N4**)$_n$ battery presented excellent rate and cycling performance, impressive stability against self-discharge and a record EE. Our findings broaden the available chemistry and enrich the option of active materials for RABs. The quaternization chemistry can be readily extended to other multivalent metal batteries. We believe that, with proper amine compounds and necessary device optimization, they are promising for building metal–amine grid batteries and flow batteries for large-scale stationary energy storage.

Acknowledgements

The authors acknowledge the CFAED and the Dresden Center for Nanoanalysis (DCN) at TU Dresden. The authors thank the Center for Information Services and High Performance Computing (ZIH) at TU Dresden for generous allocations of compute resources. This work was financially supported by European Union's Horizon 2020 research and innovation program (GrapheneCore3 881603), SPE3 project funded by German Ministry for Education and Research (BMBF) under Forschung für neue Mikroelektronik (ForMikro) program, M-ERA.NET and Sächsisches Staatsministerium für Wissenschaft und Kunst (HYSUCAP 100478697), and CRC 1415 (Grant No. 417590517). Open Access funding enabled and organized by Projekt DEAL.

Conflict of Interest

The authors declare no conflict of interest.

Data Availability Statement

The data that support the findings of this study are available from the corresponding author upon reasonable request.

Keywords: Al-Ion Batteries · Amine · Anion Storage · Quaternization

[1] D. Larcher, J. M. Tarascon, *Nat. Chem.* **2015**, *7*, 19.
[2] a) E. Faegh, B. Ng, D. Hayman, W. E. Mustain, *Nat. Energy* **2021**, *6*, 450–450; b) D. J. Kim, D.-J. Yoo, M. T. Otley, A. Prokofjevs, C. Pezzato, M. Owczarek, S. J. Lee, J. W. Choi, J. F. Stoddart, *Nat. Energy* **2019**, *4*, 51–59.
[3] H. Yang, H. Li, J. Li, Z. Sun, K. He, H. M. Cheng, F. Li, *Angew. Chem. Int. Ed.* **2019**, *58*, 11978–11996; *Angew. Chem.* **2019**, *131*, 12104–12124.
[4] a) B. J. Hopkins, Y. Shao-Horn, D. P. Hart, *Science* **2018**, *362*, 658–661; b) J. Ryu, H. Jang, J. Park, Y. Yoo, M. Park, J. Cho, *Nat. Commun.* **2018**, *9*, 3715.
[5] a) T. Gao, X. Li, X. Wang, J. Hu, F. Han, X. Fan, L. Suo, A. J. Pearse, S. B. Lee, G. W. Rubloff, K. J. Gaskell, M. Noked, C. Wang, *Angew. Chem. Int. Ed.* **2016**, *55*, 9898–9901; *Angew. Chem.* **2016**, *128*, 10052–10055; b) H. Yang, L. Yin, J. Liang, Z. Sun, Y. Wang, H. Li, K. He, L. Ma, Z. Peng, S. Qiu, C. Sun, H. M. Cheng, F. Li, *Angew. Chem. Int. Ed.* **2018**, *57*, 1898–1902; *Angew. Chem.* **2018**, *130*, 1916–1920; c) G. Cohn, L. Ma, L. A. Archer, *J. Power Sources* **2015**, *283*, 416–422.
[6] Z. Lin, M. Mao, C. Yang, Y. Tong, Q. Li, J. Yue, G. Yang, Q. Zhang, L. Hong, X. Yu, L. Gu, Y.-S. Hu, H. Li, X. Huang, L. Suo, L. Chen, *Sci. Adv.* **2021**, *7*, eabg6314.
[7] a) M.-C. Lin, M. Gong, B. Lu, Y. Wu, D.-Y. Wang, M. Guan, M. Angell, C. Chen, J. Yang, B.-J. Hwang, H. Dai, *Nature* **2015**, *520*, 324–328; b) H. Chen, H. Xu, S. Wang, T. Huang, J. Xi, S. Cai, F. Guo, Z. Xu, W. Gao, C. Gao, *Sci. Adv.* **2017**, *3*, eaao7233; c) G. Wang, M. Yu, J. Wang, D. Li, D. Tan, M. Loffler, X. Zhuang, K. Mullen, X. Feng, *Adv. Mater.* **2018**, *30*, 1800533.
[8] a) Y. Song, S. Jiao, J. Tu, J. Wang, Y. Liu, H. Jiao, X. Mao, Z. Guo, D. J. Fray, *J. Mater. Chem. A* **2017**, *5*, 1282–1291; b) M. Han, Z. Lv, L. Hou, S. Zhou, H. Cao, H. Chen, Y. Zhou, C. Meng, H. Du, M. Cai, Y. Bian, M.-C. Lin, *J. Power Sources* **2020**, *451*, 227769.
[9] a) D.-J. Yoo, M. Heeney, F. Glöcklhofer, J. W. Choi, *Nat. Commun.* **2021**, *12*, 2386; b) J. Zhou, X. Yu, J. Zhou, B. Lu, *Energy Storage Mater.* **2020**, *31*, 58–63; c) S. Wang, S. Huang, M. Yao, Y. Zhang, Z. Niu, *Angew. Chem. Int. Ed.* **2020**, *59*,

11800–11807; *Angew. Chem.* **2020**, *132*, 11898–11905; d) X. Fan, F. Wang, X. Ji, R. Wang, T. Gao, S. Hou, J. Chen, T. Deng, X. Li, L. Chen, C. Luo, L. Wang, C. Wang, *Angew. Chem. Int. Ed.* **2018**, *57*, 7146–7150; *Angew. Chem.* **2018**, *130*, 7264–7268.
[10] J. Bitenc, N. Lindahl, A. Vizintin, M. E. Abdelhamid, R. Dominko, P. Johansson, *Energy Storage Mater.* **2020**, *24*, 379–383.
[11] G. Dai, Y. Liu, Z. Niu, P. He, Y. Zhao, X. Zhang, H. Zhou, *Matter* **2019**, *1*, 945–958.
[12] K. Lee, I. E. Serdiuk, G. Kwon, D. J. Min, K. Kang, S. Y. Park, J. E. Kwon, *Energy Environ. Sci.* **2020**, *13*, 4142–4156.
[13] A. K. Padhi, K. S. Nanjundaswamy, J. B. Goodenough, *J. Electrochem. Soc.* **1997**, *144*, 1188–1194.
[14] a) C. Ferrara, V. Dall'Asta, V. Berbenni, E. Quartarone, P. Mustarelli, *J. Phys. Chem. C* **2017**, *121*, 26607–26614; b) J. S. Wilkes, J. S. Frye, G. F. Reynolds, *Inorg. Chem.* **1983**, *22*, 3870–3872.
[15] K. Susumu, P. R. Frail, P. J. Angiolillo, M. J. Therien, *J. Am. Chem. Soc.* **2006**, *128*, 8380–8381.
[16] a) T. Leisegang, F. Meutzner, M. Zschornak, W. Munchgesang, R. Schmid, T. Nestler, R. A. Eremin, A. A. Kabanov, V. A. Blatov, D. C. Meyer, *Front. Chem.* **2019**, *7*, 268; b) F. Wu, H. Yang, Y. Bai, C. Wu, *Adv. Mater.* **2019**, *31*, 1806510; c) Y. Zhang, S. Liu, Y. Ji, J. Ma, H. Yu, *Adv. Mater.* **2018**, *30*, 1706310; d) D. Yuan, J. Zhao, W. Manalastas, S. Kumar, M. Srinivasan, *Nano Mater. Sci.* **2020**, *2*, 248–263.
[17] D.-Y. Wang, C.-Y. Wei, M.-C. Lin, C.-J. Pan, H.-L. Chou, H.-A. Chen, M. Gong, Y. Wu, C. Yuan, M. Angell, Y.-J. Hsieh, Y.-H. Chen, C.-Y. Wen, C.-W. Chen, B.-J. Hwang, C.-C. Chen, H. Dai, *Nat. Commun.* **2017**, *8*, 14283.
[18] D.-J. Yoo, J. W. Choi, *J. Phys. Chem. Lett.* **2020**, *11*, 2384–2392.
[19] M. Walter, K. V. Kravchyk, C. Böfer, R. Widmer, M. V. Kovalenko, *Adv. Mater.* **2018**, *30*, 1705644.
[20] a) O. Yurchenko, J. Heinze, S. Ludwigs, *ChemPhysChem* **2010**, *11*, 1637–1640; b) C. E. D. Chidsey, R. W. Murray, *J. Phys. Chem.* **1986**, *90*, 1479–1484; c) E. F. Dalton, N. A. Surridge, J. C. Jernigan, K. O. Wilbourn, J. S. Facci, R. W. Murray, *Chem. Phys.* **1990**, *141*, 143–157; d) D. Ofer, R. M. Crooks, M. S. Wrighton, *J. Am. Chem. Soc.* **1990**, *112*, 7869–7879.
[21] a) H. Hu, T. Cai, P. Bai, J. Xu, S. Ge, H. Hu, M. Wu, Q. Xue, Z. Yan, X. Gao, W. Xing, *Chem. Commun.* **2020**, *56*, 1593–1596; b) D. Han, M.-S. Cao, N. Li, D.-M. She, W.-L. Song, H. Chen, S. Jiao, D. Fang, *Chin. J. Chem.* **2021**, *39*, 157–164.
[22] V. W. Lau, I. Moudrakovski, J. Yang, J. Zhang, Y. M. Kang, *Angew. Chem. Int. Ed.* **2020**, *59*, 4023–4034; *Angew. Chem.* **2020**, *132*, 4052–4063.
[23] a) Z. Lv, M. Han, J. Sun, L. Hou, H. Chen, Y. Li, M.-C. Lin, *J. Power Sources* **2019**, *418*, 233–240; b) C. Yang, J. Chen, X. Ji, T. P. Pollard, X. Lü, C.-J. Sun, S. Hou, Q. Liu, C. Liu, T. Qing, Y. Wang, O. Borodin, Y. Ren, K. Xu, C. Wang, *Nature* **2019**, *569*, 245–250.

Manuscript received: November 27, 2021
Accepted manuscript online: January 13, 2022
Version of record online: January 24, 2022